Study on the flow nucleate boiling heat transfer of slush nitrogen

Q D Wang, X Y Lu and T Jin*

Institute of Refrigeration and Cryogenics / Zhejiang Key Laboratory of Refrigeration and Cryogenic Technology, Zhejiang University, Hangzhou 310027, China

*Corresponding author: T Jin, Email: jintao@zju.edu.cn, Tel: +86-571-87953233

Abstract. A three-dimensional numerical simulation method is developed to predict the heat transfer characteristics during the flow boiling of cryogenic slurry in horizontal circular pipes, based on Euler-Euler model with a boiling model for liquid-vapor mass transfer. The model incorporates the Ishii model for vapor-liquid interaction and the Huilin-Gidaspow model for solid-liquid interaction, also with the modification accounting for slush effective viscosity. The modification enables to simulate the effects of solid particle on bubble detachment. The model can well demonstrate the heat transfer characteristics of subcooled liquid hydrogen, and also the solid phase distribution in slush nitrogen pipe flow. The simulation results show that an increased heat flux can result in a higher vapor volume fraction at the wall and a corresponding decrease in solid volume fraction. At low heat flux, an increase in solid volume fraction enhances the boiling heat transfer, while at higher flux, the solid phase suppresses the heat transfer. Consistent trends are observed in both bottom and surrounding heating layouts. Furthermore, turbulence analysis shows that solid particles can increase turbulent kinetic energy near the wall but inhibit its diffusion toward the pipe center, which indicates that the bubbles will induce the solid particles to accumulate toward the pipe center, while the solid particles inhibit the bubbles releasing from the pipe wall, thereby suppressing the boiling heat transfer.

1. Introduction

Slush nitrogen is a solid-liquid two-phase fluid, its cooling capacity is larger than that of liquid nitrogen thanks to the solid particles with melting latent heat [1]. Slush nitrogen can be a promising coolant for the high-temperature superconducting (HTS) cables [2]. However, the heat transfer characteristics of slush nitrogen have not been fully understood. Specifically, flow boiling is crucial in the application of slush nitrogen, which can provide important judgment for the quenching of HTS cables.

Flow boiling phenomena can be categorized into two primary modes based on thermal boundary conditions [3]. At low wall heat flux, bubbles form within the bulk liquid due to progressive heat accumulation along the flow pipe, typically in systems with subcooled liquid and moderate thermal gradients. This contrasts with flow nucleate boiling, where high wall superheat triggers instantaneous bubble generation directly at the heating wall through rapid heterogeneous nucleation, bypassing bulk liquid heating stages. The distinction primarily depends on whether phase change initiates in the liquid bulk (low heat flux) or at the heating wall (high heat flux).

This study employs CFD to resolve three-phase (liquid-solid-vapor) interactions in slush nitrogen flow nucleate boiling. We quantify how solid particle concentration alters boiling heat

Content from this work may be used under the terms of the Creative Commons Attribution 4.0 licence. Any further distribution of this work must maintain attribution to the author(s) and the title of the work, journal citation and DOI.
Published under licence by IOP Publishing Ltd

transfer at varying heat fluxes. The model integrates phase-change dynamics with particle-induced nucleation enhancement and bubble mobility suppression mechanisms. Results reveal critical correlations between thermal-hydraulic parameters, particle-bubble interactions and boiling efficiency.

2. Mathematical and physical models

This study addresses the multiphase coupling mechanisms in horizontal pipe flow nucleate boiling of slush nitrogen, where forced convection, non-horizontal heating wall, and confined bubble detachment coexist. The solid-liquid flow pattern critically influences boiling behavior: at Re_{sl}<25000 (slip-bed flow), particles accumulate near the pipe bottom (figure 1a), while Re_{sl}>25000 (pseudo-homogeneous flow) induces axial particle migration (figure 1b) [4]. Solid particles exhibit dual thermal effects – latent heat absorption during melting enhances heat transfer, while increased slush effective viscosity promotes bubble-wall adhesion that degrades boiling efficiency.

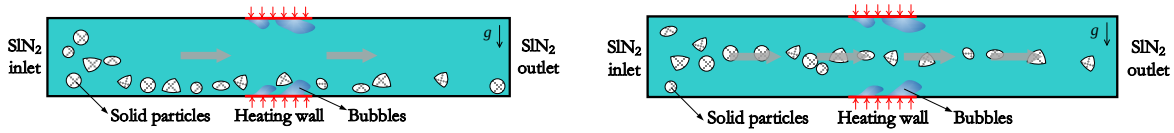

(a) slip-bed flow (Re_{sl}<25000) (b) pseudo-homogeneous flow (Re_{sl}≥25000)

Figure 1. Physical model of cryogenic slurry flow nucleate boiling in a pipe

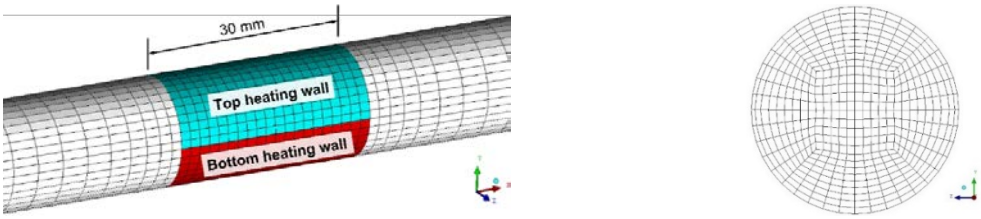

(a) heating wall mesh (b) pipeline section mesh

Figure 2. Three-dimensional structured meshing

A 16-mm-diameter, 0.8-m-long horizontal pipe (50D hydrodynamic development length) is modeled with conjugate heat transfer analysis. Gravity acts along the negative y-axis. Heating wall (30 mm axial length) are partitioned at the top and bottom pipe cross-sections to capture radial heat transfer asymmetry. Wall boundary layers are resolved at y+ ≈ 30 using 0.4-mm-thick prism cells. Key assumptions include:

1) Solid-phase sphericity with fixed diameter (1.5 mm).
2) Pressure-dependent saturation temperature (77.3 K at 101 kPa).
3) Phase-change thresholds (melting at 63.2 K, boiling at 77.3 K).
4) Critical heat flux (CHF) happens at vapor volume fraction >80% at wall-adjacent cells [5].
5) Negligible vapor-solid direct interactions.

3. Numerical method

3.1. Governing equation

The volume fractions of three phases satisfy

$$\alpha_s + \alpha_l + \alpha_v = 1 \quad (1)$$

The governing equations for solid(s)-liquid(l)-vapor(v) multiphase flow are formulated for individual phases, and the equations of Continuity, Momentum and Energy are as followed

$$\frac{\partial}{\partial t}(\alpha_j\rho_j) + \nabla\cdot(\alpha_j\rho_j\vec{v}_j) = \sum_{i=1}^{n}(\dot{m}_{ij} - \dot{m}_{ji}) \tag{2}$$

$$\frac{\partial}{\partial t}(\alpha_j\rho_j\vec{v}_j) + \nabla\cdot(\alpha_j\rho_j\vec{v}_j\vec{v}_j) = -\alpha_j\nabla P + \nabla\cdot\bar{\bar{\tau}}_j + \alpha_j\rho_j\vec{g} + \sum_{i=1}^{n}(\vec{R}_{ij} + \dot{m}_{ij}\vec{v}_{ij} - \dot{m}_{ji}\vec{v}_{ji}) \tag{3}$$

$$\frac{\partial}{\partial t}(\alpha_j\rho_j h_j) + \nabla\cdot(\alpha_j\rho_j\vec{v}_j h_j) = -\alpha_j\frac{\partial P_j}{\partial t} + \bar{\bar{\tau}}_j:\nabla\vec{v}_j + \nabla\cdot\vec{q}_j + \sum_{i=1}^{n}(Q_{ij} + \dot{m}_{ij}h_i - \dot{m}_{ji}h_j) \tag{4}$$

For liquid phase (j=l), interaction terms involve solid (i=1) and vapor (i=2) phases. Interphase forces $\vec{R}_{ij}$ include drag, lift, and virtual mass effects. The stress tensor $\bar{\bar{\tau}}_j$ follows Newtonian fluid assumptions. Solid particles are simulated using the particle dynamic theory, with configurations for granular temperature and other parameters following the approach described in Ref.[6].

Following Vadlamudi & Nayak [7], the Realizable k-ε model with Standard Wall Function is adopted for its superior prediction of CHF in nucleate boiling. Turbulence parameters are treated using the Per Phase approach, as validated by Zhang et al. [8] for subcooled boiling simulations.

3.2. Interphase force modeling

According to the assumption 5), interphase drag and lift forces are modelled with viscosity corrections to account for solid effects, where solid-vapor interactions are implicitly addressed through modified slush effective viscosity μ_{sl} [6].

Solid-liquid drag K_{sl} follows the Huilin-Gidaspow model [9] with μ_{sl} substitution:

$$K_{\mathrm{sl}} = \begin{cases} \frac{3}{4}C_{\mathrm{D,sl}}\frac{\alpha_{\mathrm{s,e}}\alpha_{\mathrm{l,e}}\rho_{\mathrm{l}}|\vec{v}_{\mathrm{s}} - \vec{v}_{\mathrm{l}}|}{d_{\mathrm{s}}}\alpha_{\mathrm{l,e}}^{-2.65}, & \alpha_{\mathrm{s}} < 0.2 \\ 150\frac{\alpha_{\mathrm{s,e}}^2\mu_{\mathrm{sl}}}{\alpha_{\mathrm{l,e}}d_{\mathrm{s}}^2} + 1.75\frac{\alpha_{\mathrm{s,e}}\rho_{\mathrm{l}}|\vec{v}_{\mathrm{s}} - \vec{v}_{\mathrm{l}}|}{d_{\mathrm{s}}}, & \alpha_{\mathrm{s}} \geq 0.2 \end{cases} \tag{5}$$

where $C_{\mathrm{D,sl}} = \max\left[\frac{24}{Re_{\mathrm{sl}}}\left(1 + 0.15Re_{\mathrm{sl}}^{0.687}\right), 0.44\right]$ and $Re_{\mathrm{sl}} = \frac{\rho_{\mathrm{l}}|\vec{v}_{\mathrm{s}} - \vec{v}_{\mathrm{l}}|d_{\mathrm{s}}}{\mu_{\mathrm{sl}}}$. Effective volume fractions $\alpha_{i,\mathrm{e}} = \alpha_i/(\alpha_i + \alpha_j)$ ensure phase fraction consistency.

Liquid-vapor drag K_{lv} follows the Ishii model [10] modified with μ_{sl}:

$$K_{\mathrm{lv}} = \frac{\mu_{\mathrm{sl}}C_{\mathrm{D,lv}}Re_{\mathrm{lv}}}{8d_{\mathrm{v}}^2} \tag{6}$$

where $C_{\mathrm{D,lv}} = \min\left[\frac{24}{Re_{\mathrm{lv}}}\left(1 + 0.15Re_{\mathrm{lv}}^{0.75}\right), \frac{2}{3}\frac{d_{\mathrm{v}}}{\sqrt{\frac{\sigma}{g|\rho_{\mathrm{l}} - \rho_{\mathrm{v}}|}}}\right]$ and $Re_{\mathrm{lv}} = \frac{\rho_{\mathrm{l}}|\vec{v}_{\mathrm{v}} - \vec{v}_{\mathrm{l}}|d_{\mathrm{v}}}{\mu_{\mathrm{sl}}}$.

3.3. Heat and mass transfer models

The framework aims at resolving the phase transitions, bubble dynamics, and heat partitioning in cryogenic three-phase flows. A modified RPI boiling model incorporates the vapor-wall heat transfer:

$$\dot{q}_{\mathrm{W}} = \left(\dot{q}_{\mathrm{C}} + \dot{q}_{\mathrm{Q}} + \dot{q}_{\mathrm{E}}\right)f(\alpha_{\mathrm{l}}) + [1 - f(\alpha_{\mathrm{l}})]\dot{q}_{\mathrm{V}} \tag{7}$$

where convective heat flux $\dot{q}_{\mathrm{C}} = h_{\mathrm{C}}(T_{\mathrm{w}} - T_{\mathrm{l}})(1 - A_{\mathrm{b}})$, quenching heat flux $\dot{q}_{\mathrm{Q}} = \frac{2k_{\mathrm{l}}}{\sqrt{\pi a_{\mathrm{l}}\tau}}(T_{\mathrm{w}} - T_{\mathrm{l}})$, evaporative heat flux $\dot{q}_{\mathrm{E}} = \frac{\pi d_{\mathrm{b}}^3}{6} N_{\mathrm{w}} \rho_{\mathrm{v}} \Delta h_{\mathrm{lv}} f_{\mathrm{b}}$ and vapor-wall heat flux $\dot{q}_{\mathrm{V}} = h_{\mathrm{V}}(T_{\mathrm{w}} - T_{\mathrm{v}})$.

Transition function $f(\alpha_{\mathrm{l}})$ switches at $\alpha_{\mathrm{l,crit}} = 0.2$:

$$f(\alpha_{\mathrm{l}}) = \begin{cases} 1 - 0.5\exp\left[-20\left(\alpha_{\mathrm{l}} - \alpha_{\mathrm{l,crit}}\right)\right], & \alpha_{\mathrm{l}} \geq \alpha_{\mathrm{l,crit}} \\ 0.5\left(\alpha_{\mathrm{l}}/\alpha_{\mathrm{l,crit}}\right)^{20\alpha_{\mathrm{l,crit}}}, & \alpha_{\mathrm{l}} < \alpha_{\mathrm{l,crit}} \end{cases} \tag{8}$$

Bubble diameter d_b and frequency f_{b} follow Zhang et al. [11]:

$$d_b = \begin{cases} 0.001 \times (0.007Ja^2 - 0.024Ja + 0.92), & Ja \leq 10.8 \\ 0.0001 \times (2.526Ja^2 - 64.74Ja + 437.63), & Ja \geq 12.2 \end{cases} \tag{9}$$

$$f_{\mathrm{b}} = \begin{cases} 1.68857^2 Ja^2/1000d_b^2, & Ja \leq 10.8 \\ 3.71287^2 Ja^2/10000d_b^2, & Ja \geq 12.2 \end{cases} \tag{10}$$

Other key parameters of the boiling model can refer to reference [12].

4. Results and discussion

Figure 3 presents the vapor (a) and solid (b) volume fraction distributions in slush nitrogen (24% solid fraction) flow nucleate boiling within a 16-mm horizontal pipe (z=0 cross-section). Simulations at inlet velocity 1 m/s and outlet pressure 101 kPa compare four bottom-heated cases (240–510 kW/m^2).

In figure 3a, the elevated heat flux promotes near-wall vapor accumulation, with downstream vapor concentrations exceeding upstream values, which indicates progressive thermal boundary layer development along the heating wall. Per assumption 4), nucleate boiling crisis occurs when local vapor volume fraction exceeds 80% (red region), triggering transition to film boiling. The cross-section of x=0.415 m serves as the critical monitoring location for maximum vapor volume fraction.

Figure 3b exhibit sharp near-wall interfaces, coinciding with vapor boundaries in figure 3a. Vapor-dominated zones expands at increased heat flux, promoting solids towards the pipe axis. This phase-segregation pattern confirms strong vapor-solid interaction mediated by slush effective viscosity gradients. The vapor-solid interface alignment demonstrates particle exclusion effects driven by bubble-induced shear stresses during boiling.

Figure 4 compares vapor volume fraction contours at x=0.415 m for slush nitrogen with solid volume fractions of 0%, 11.5%, and 24%. Case (a) employs bottom heating (510 kW/m^2), while case (b) utilizes surrounding heating (330 kW/m^2). Higher solid volume fractions promote vapor accumulation near the bottom heating wall (figure 4a), indicating proximity to the nucleate boiling critical point. This trend also occurs under surrounding heating (figure 4b), where vapor enrichment correlates with solid volume fraction. The intensified phase separation under elevated solid fractions demonstrates particle-mediated suppression of bubble detachment, promoting localized vapor retention.

Nucleate boiling curves for slush nitrogen (solid fractions: 0%, 11.5%, 24%) at the inlet velocity of 1 m/s and the pressure of 101 kPa reveal distinct heat transfer regimes. For bottom heating (figure 5a), heat transfer coefficients increase with solid fraction at low heat fluxes (<150 kW/m^2) but decrease at high heat fluxes (>150 kW/m^2). This reversal also occurs under surrounding heating (figure 5b), indicating that elevated solid fractions enhance slush effective

viscosity at high heat fluxes, hence suppressing bubble nucleation/detachment and reducing heat transfer coefficients.

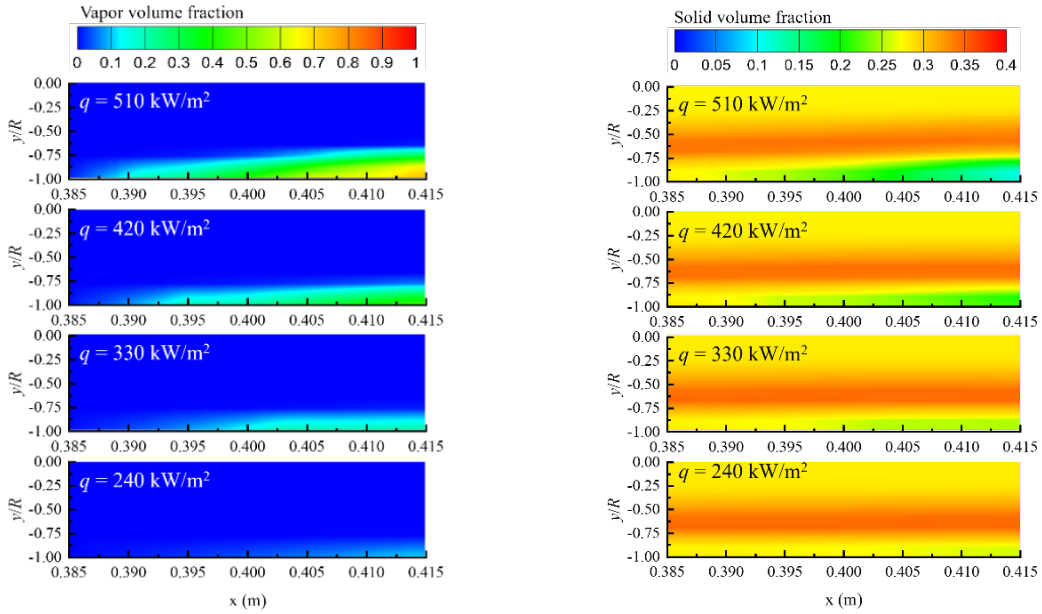

(a) vapor distribution (b) solid distribution

Figure 3. Evolution of solid and vapor phase distribution cloud charts during bottom heating

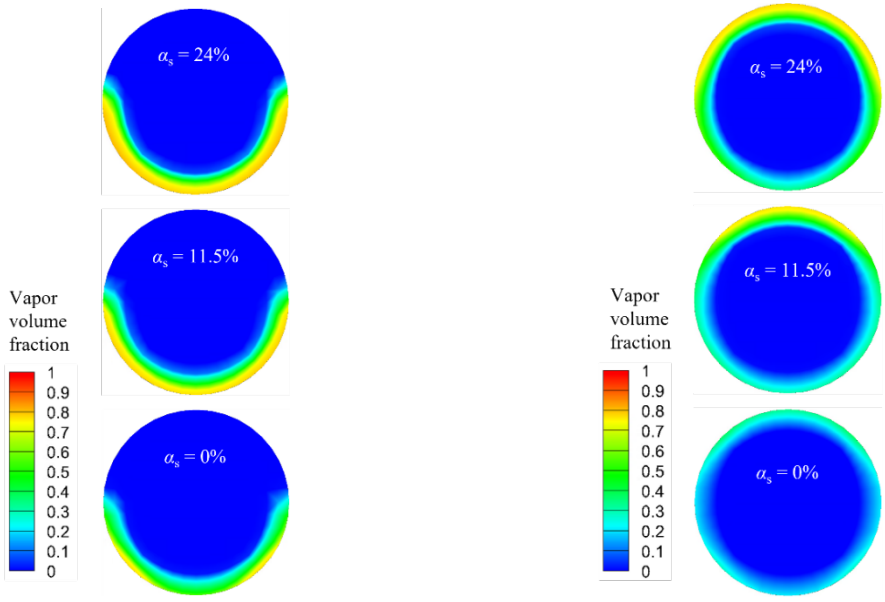

(a) bottom heating (q=510 kW/m²) (b) surrounding heating (q=330 kW/m²)

Figure 4. Cloud chart of vapor phase distribution in pipe cross-section

Maximum vapor volume fraction at the heating wall decreases with the increasing solid fractions (figure 6a and 6b). Higher solid fractions elevate wall superheat at CHF, which can be attributed to:

1) Viscosity-driven bubble adhesion: Increased slurry viscosity impedes bubble detachment, amplifying near-wall thermal resistance.

2) Latent heat absorption: Particle melting consumes vaporization energy, accelerating vapor condensation.
3) Dual-phase thermal inertia: Liquid-phase heating must overcome both sensible heat and melting energy, reducing vapor generation efficiency.

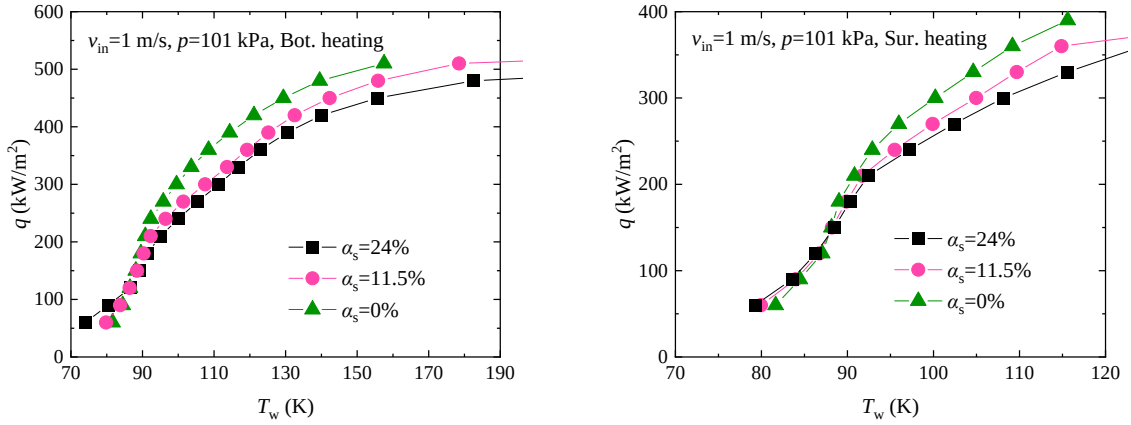

(a) bottom heating (b) surrounding heating

Figure 5. Numerical flow nucleate boiling curves of SlN_2 with various solid volume fractions

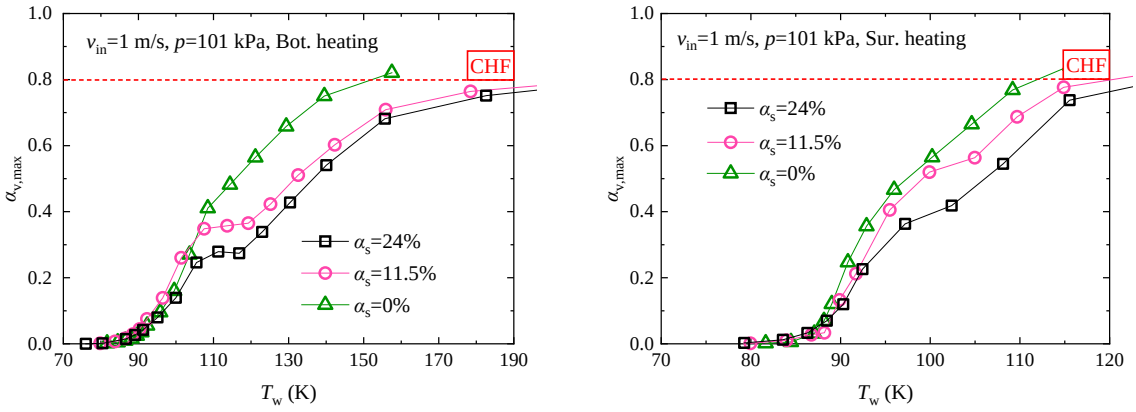

(a) bottom heating (b) surrounding heating

Figure 6. Maximum vapor volume fraction on the wall under various solid volume fractions

Using an 80% vapor volume fraction threshold for boiling crisis detection, Figure 7 quantifies CHF and wall temperature variations with solid volume fraction (0%–30%). Bottom heating yields CHF = 479–521 kW/m^2 and wall temperatures = 142–235 K, while surrounding heating shows CHF = 320–372 kW/m^2 and temperatures = 103–135 K. CHF decreases with increasing solid volume fraction, whereas critical wall temperature rises, reflecting enhanced thermal resistance from particle-induced viscosity and phase interactions.

For 15% solid volume fraction flow (1 m/s), figure 8 compares heated (150 kW/m^2 surrounding) and unheated cases. The core solid volume fraction increases from 22.5% to 25%, while near-wall iso-concentration lines (5% top, 10% bottom) converge toward the axis. This redistribution suggests vapor-phase expansion generates inward-directed forces on solids via momentum transfer during boiling. Enhanced solid concentration gradients in the lower pipe half further confirm vapor-solid interactions. Solid melting and particle migration occur concurrently.

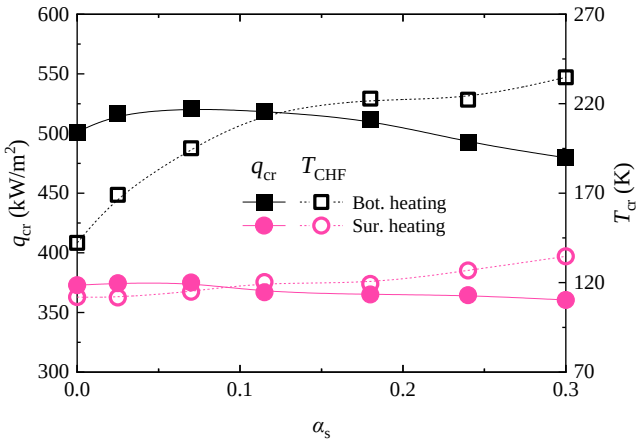

Figure 7. CHF and wall temperature at CHF under various solid volume fractions

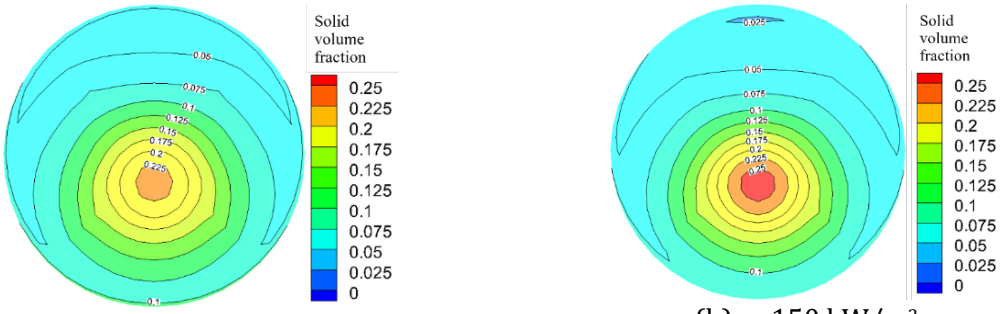

(a) q=0 kW/m^2 (b) q=150 kW/m^2

Figure 8. Cloud chart of solid phase distribution in pipe cross-section

Turbulence profiles at x = 0.415 m (bottom heating, 150 kW/m^2) show elevated near-wall turbulent kinetic energy with increasing solid volume fraction (figure 9). Steeper turbulent kinetic energy gradients correlate with higher solid fractions, indicating particle-induced turbulence amplification. Vapor-driven inward particle forces and outward vapor resistance jointly suppress thermal diffusion to the axis. This bidirectional phase coupling reduces heat transfer efficiency by weakening particle deposition and enhancing vapor adhesion at heating wall.

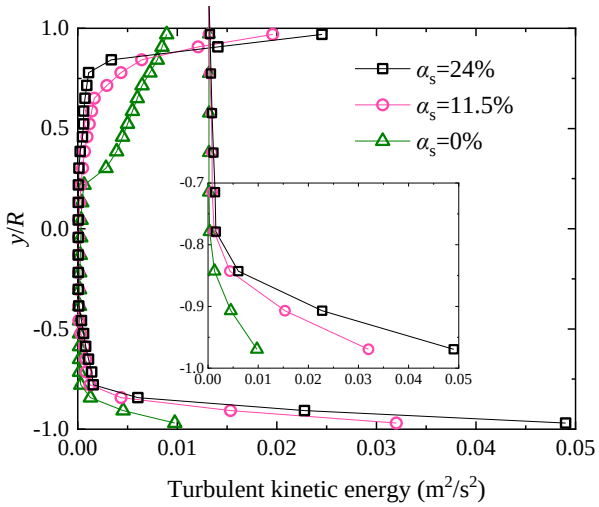

Figure 9. CFD results of kinetic turbulent energy near the wall

5. Conclusions

This study develops a numerical framework using a Euler-Euler approach with modified boiling models to simulate flow nucleate boiling heat transfer of slush nitrogen in horizontal pipes. The model integrates viscosity-corrected interphase force models (Ishii for vapor-liquid, Huilin-Gidaspow for solid-liquid) to capture particle-induced suppression of bubble detachment, coupled with solid-liquid phase-change equations to resolve melting effects.

Numerical results demonstrate that increasing heat flux elevates near-wall vapor volume fractions while reducing solid volume fractions. Solid particles exhibit dual heat transfer effects: enhancement at low heat fluxes (<150 kW/m^2) via turbulence modulation and suppression at high heat fluxes (>150 kW/m^2) due to viscosity-driven bubble adhesion. Both bottom and surrounding heating configurations reveal consistent trends, with particle migration toward the pipe axis under vapor expansion forces and suppressed thermal diffusion due to bidirectional phase interactions. Turbulence analysis further highlights that higher solid fractions amplify near-wall turbulent kinetic energy but inhibit its radial propagation, correlating with localized heat accumulation and reduced heat transfer efficiency.

These findings elucidate the coupled mechanisms of particle-vapor interactions in cryogenic slurry boiling, emphasizing the critical role of solid fraction in regulating phase redistribution and thermal resistance. The insights provide a foundation for optimizing heat transfer performance in applications such as superconducting cooling, where slush nitrogen's multiphase behaviour governs system efficiency and stability.

Acknowledgments

This work is financially supported by Basic Research Funds for the Central Government 'Innovative Team of Zhejiang University' under contract number (2022FZZX01-09).

References

[1] Ma F, Zhang P 2020 *Energy* **192** 116602
[2] Ishimoto J, Ohno R, Yanagi H, Machida 2004 *AIP Conference Proceedings* **710** 1099–1106
[3] Kim S M, Mudawar I 2013 *International Journal of Heat and Mass Transfer* **64** 1226–1238
[4] Jiang Y Y, Zhang P 2012 *AIChE J* **59** 1762–1773
[5] Zhang Y P, Zhang R, Tian W X, Su G H, Qiu S Z 2019 *Applied Thermal Engineering* **149** 881–888
[6] Jin T, Li Y J, Wu S Q, Liu Y L 2017 *Applied Thermal Engineering* **123** 301–309
[7] Vadlamudi S R G, Nayak A K 2019 *Nuclear Engineering and Design* **352** 110150
[8] Zhang R, Cong T, Tian W, Qiu S Z, Su G H 2015 *Annals of Nuclear Energy* **80** 293–302
[9] Huilin L, Gidaspow D 2003 *Chemical Engineering Science* **58** 3777–3792
[10]Ishii M 1990 *Multiphase Science and Technology* **5** 1–4
[11]Zhang X B, Xiong W, Chen J Y 2015 *Physics Procedia* **67** 569–575
[12]Wu S Q, Wang Q D, Li Y J, Huang J L, Jin T 2020 *IOP Conference Series: Materials Science and Engineering* **755** 012026